

PAPER • OPEN ACCESS

Achieving precise graphenization of diamond coatings below the interfacial thermal stress threshold

To cite this article: Bo Yan *et al* 2025 *Int. J. Extrem. Manuf.* **7** 015106

View the [article online](#) for updates and enhancements.

You may also like

- [Towards atomic-scale smooth surface manufacturing of -Ga₂O₃ via highly efficient atmospheric plasma etching](#)
Yongjie Zhang, Yuxi Xiao, Jianwen Liang et al.
- [A review for design, mechanism, fabrication, and application of magnetically responsive microstructured functional surface](#)
Jian Wang, Xingyi Song, Chaochao Wang et al.
- [Advanced multi-nozzle electrohydrodynamic printing: mechanism, processing, and diverse applications at micro/nano-scale](#)
Yin Li, Guangming Zhang, Jinrun Zhang et al.

Achieving precise graphenization of diamond coatings below the interfacial thermal stress threshold

Bo Yan¹, Ning He¹, Ni Chen^{1,*} , Matthias Weigold², Huiwen Chen¹, Shuchen Sun¹, Yang Wu¹, Shiyang Fu¹, Liang Li¹ and Eberhard Abele²

¹ College of Mechanical and Electrical Engineering, Nanjing University of Aeronautics and Astronautics, Nanjing 210016, People's Republic of China

² Institute of Production Management, Technology and Machine Tools (PTW), Technical University of Darmstadt, Otto-Berndt-Straße 2, Darmstadt 64287, Germany

E-mail: ni.chen@nuaa.edu.cn

Received 21 May 2024, revised 30 July 2024

Accepted for publication 30 October 2024

Published 14 November 2024



Abstract

Diamond coatings possess numerous excellent properties, making them desirable materials for high-performance surface applications. However, without a revolutionary surface modification method, the surface roughness and friction behavior of diamond coatings can impede their ability to meet the demanding requirements of advanced engineering surfaces. This study proposed the thermal stress control at coating interfaces and demonstrated a novel process of precise graphenization on conventional diamond coatings surface through laser induction and mechanical cleavage, without causing damage to the metal substrate. Through experiments and simulations, the influence mechanism of surface graphitization and interfacial thermal stress was elucidated, ultimately enabling rapid conversion of the diamond coating surface to graphene while controlling the coating's thickness and roughness. Compared to the original diamond coatings, the obtained surfaces exhibited a 63%–72% reduction in friction coefficients, all of which were below 0.1, with a minimum of 0.06, and a 59%–67% decrease in specific wear rates. Moreover, adhesive wear in the friction counterpart was significantly inhibited, resulting in a reduction in wear by 49%–83%. This demonstrated a significant improvement in lubrication and inhibition of mechanochemical wear properties. This study provides an effective and cost-efficient avenue to overcome the application bottleneck of engineered diamond surfaces, with the potential to significantly enhance the performance and expand the application range of diamond-coated components.

Supplementary material for this article is available [online](#)

Keywords: diamond coating, graphene, laser, thermal stress, lubrication and anti-wear

* Author to whom any correspondence should be addressed.



Original content from this work may be used under the terms of the [Creative Commons Attribution 4.0 licence](#). Any further distribution of this work must maintain attribution to the author(s) and the title of the work, journal citation and DOI.

1. Introduction

Conventional diamond coatings produced by chemical vapor deposition (CVD) possess numerous excellent properties that are comparable to, or even surpass, natural diamonds. These properties include extremely high hardness, exceptional thermal conductivity, high wear resistance, and excellent chemical stability [1, 2]. Furthermore, the preparation of CVD diamond coatings is not limited by the shape of the substrate, allowing for direct deposition onto complex-shaped surfaces. These outstanding characteristics make them an ideal material for high-performance coating applications, and they have been widely employed in various fields such as cutting tools, mechanical seals, wire drawing dies, and bearings, where lubrication and wear resistance are essential for sliding friction surfaces [3, 4]. The grain sizes of conventional diamond coatings were in the micron range, with extremely high hardness, good elastic modulus, high crystallinity and strong substrate adhesion, which are highly significant for their engineering surface applications [5, 6]. However, the thickness of untreated conventional diamond coatings is uneven, and the surface roughness is large, resulting in poor interfacial friction state [7]. These shortcomings make it difficult to meet the demanding requirements for developing high-performance engineering surfaces, severely limiting the further extensive application of diamond coatings.

Currently, extensive research is dedicated to addressing the challenges faced by conventional diamond coatings in achieving wider applications. Two main strategies can be distinguished from whether the grain size of the diamond coating changes: modifying the grain size of the diamond coating and surface planarization techniques. The first strategy involves controlling the CVD process parameters to reduce the grain size of the deposited diamond coating [8]. As the grain size decreases, the surface roughness of the diamond coating also decreases, leading to an improvement in the corresponding interfacial friction state. However, reducing the grain size results in an increased interfacial area, primarily composed of amorphous carbon phases, significantly reducing the adhesion of the diamond coating to the substrate and its hardness [9]. Although multilayer composite diamond coatings exhibit good impact resistance, substrate adhesion, and interfacial friction state, the thickness of the coating and the complexity of the deposition process pose significant obstacles to their widespread engineering applications [10]. The second strategy involves surface planarization techniques, including mechanical polishing, thermochemical polishing, chemical-assisted mechanical polishing, ion beam polishing, and laser polishing [11]. The first three methods mentioned are contact-based polishing techniques. Although they can significantly reduce the surface roughness of diamond coatings and enhance their performance, they are limited to planar and spherical surfaces, with limited polishing efficiency [12]. Moreover, due to the thinness of diamond coatings, the inherent prolonged impact and vibration in contact-based polishing processes inevitably lead to damage of diamond coatings [12]. Ion beam polishing and laser polishing methods are non-contact polishing

techniques that can avoid the above problems and are capable of polishing irregular samples. However, ion beam polishing is limited by the size of the reaction chamber, making it unsuitable for polishing large-area diamond coatings [11]. Additionally, it involves complex operations and incurs high polishing costs. Laser polishing is the fastest method among all diamond coating polishing techniques and has advantages such as chemically clean polished surfaces [13]. From the fundamental interaction between laser and diamond, laser polishing can be categorized into thermal polishing and cold polishing [14, 15]. Although thermal laser polishing has low polishing costs, it often leaves behind a graphitized layer on the polished surface due to localized thermal effects. This layer needs to be removed through additional annealing or acid washing [16]. Moreover, the localized transient thermal impact can potentially cause the diamond coating to burn through or delaminate. Cold laser polishing, with a pulse duration shorter than the thermal diffusion time, can achieve one-step polishing without surface graphitization [14]. However, the high equipment costs associated with cold laser polishing somewhat limit its development. Although existing polishing methods can achieve satisfactory polishing results, the performance improvements are very limited. For example, polishing to a surface roughness of 80–116 nm still results in relatively high average coefficient of friction (COF, 0.1–0.6) when facing various friction counterparts (ruby, steel and aluminum) [17–20]. Only when polished to the extreme limit of 5 nm does the average COF reach a minimum of 0.07 [18], but this is not cost-effective and cannot be applied to complex-shaped parts.

Recently, depositing graphene on the diamond surface as a solid lubricant to enhance the performance of diamond surface has been considered as a promising approach [21]. This method can be classified into two categories based on the transfer process: external transfer and in situ generation. Graphene prepared through the external transfer strategy exhibits weak adhesion strength with the diamond substrate, and under low loads, it can be easily removed after several hundreds of reciprocating friction cycles [22]. In situ generation strategies for graphene are primarily based on the CVD principle [23]. The graphene synthesized using this method generally exhibits high adhesion strength with the substrate. Won *et al* [24] successfully deposited multilayer graphene on large copper substrates using CVD method. Under a constant load of 20 mN and dry friction, these graphene layers remained intact throughout thousands of reciprocating friction cycles. Moreover, the CVD strategy enables the synthesis of covalently bonded graphene with diamond substrates. Ji *et al* [25] employed molten gallium as a catalyst and generated vertically aligned graphene covalently bonded to diamond substrates using CVD method. Even after 72 000 friction cycles under a 3 N load, the obtained surface maintained excellent lubricating properties, indicating that covalent bonding at the interface significantly enhances the durability of the surface lubrication. However, the widespread application of in situ growth strategies on diamond coatings may be hindered by the requirement of prolonged high-temperature preparation conditions [23]. This limitation arises from the low coefficient

of thermal expansion of diamond coatings compared to other substrate materials, making the diamond coating susceptible to fall off under large temperature differentials at high temperatures. Additionally, graphene has been proven to have the significant potential in effectively reducing the mechanochemical wear of diamond surfaces [26]. Chu *et al* [27] used molecular dynamics simulations to elucidate the mechanisms by which graphene acts as a physical barrier and sacrificial transfer layer to suppress the mechanochemical wear of diamond surfaces. Compared to conditions without graphene, the presence of graphene can reduce the wear of diamond tools by 34%–96%. In conclusion, seeking a cost-effective and environmentally friendly strategy to enhance the performance of conventional diamond coatings would greatly promote the application and development of diamond engineering surfaces.

We previously reported an efficient and low-energy strategy for generating covalently bonded graphene on diamond surface through laser-induced graphitization and mechanical cleavage, focusing on the instantaneous transformation of *in-situ* graphene on diamond thick film surfaces [28]. Diamond coatings have the potential to be high-performance surface materials as they can be deposited on complex-shaped substrates, offering broader application possibilities compared to diamond thick films. However, controlling the graphenization process poses significant challenges due to the extremely low thickness and substantial physical property differences between diamond coatings and metal substrates. Therefore, this study proposes that the key to overcoming this challenge lies in controlling the interfacial thermal stress below a threshold and achieving thermal smoothing during the laser induction process. Firstly, the graphitization state of diamond coatings under different laser parameters was investigated. Subsequently, a numerical model based on temperature and thermal stress fields was established to calculate the interfacial thermal stress under various laser parameters. Furthermore, through a combination of experiments and theoretical models, the influence mechanism of surface graphitization and interfacial thermal stress was elucidated, and a control method is proposed to achieve precise graphenization of the diamond coating surface. Finally, the friction characteristics of the resulting surface were evaluated under heavy load and dry friction conditions and compared with those of the original diamond coatings.

2. Experimental conditions and procedure

2.1. Graphenization of diamond coating surfaces

The conventional diamond coatings used in this study were prepared by hot filament CVD method with a deposition rate was of $0.5 \mu\text{m}\cdot\text{h}^{-1}$. The substrate for the coating was YG6 cemented carbide with a thickness of 2 mm. Prior to deposition, the cemented carbide substrate underwent mirror polishing treatment to ensure the diamond coating had a well-defined contour. The final deposited diamond coating had a thickness of $9 \mu\text{m}$ and dimensions of $10 \times 8 \text{ mm}$. The grain size was

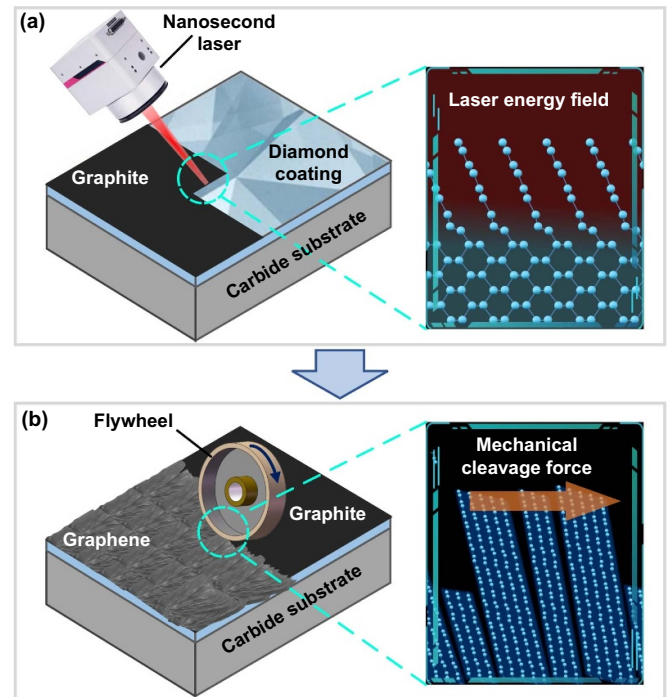


Figure 1. Schematic diagram of the precise graphenization process on diamond coating surface. (a) Laser induction. (b) Mechanical cleavage.

in the micrometer range, and the surface roughness S_a was $0.7 \mu\text{m}$.

The diamond-coated samples before graphitization were ultrasonically cleaned in absolute ethanol to remove surface impurities (figure S1). To ensure stable graphitization, a nanosecond laser (pulse width: 100 ns, spot diameter: $60 \mu\text{m}$, wavelength: 1064 nm, repetition frequency: 20 kHz, typical Gaussian beam) was employed to machine the diamond coating surface (figure 1(a)), with the process monitored using a charge coupled device camera. To achieve uniformly flat graphitization, a small and consistent movement interval ($2 \mu\text{m}$) of the pulse spot in both the scanning speed and fill spacing directions was maintained. Due to the thinness of the diamond coating, the instantaneous high temperature during the laser induction process could easily generate excessive thermal stress at the interface. Therefore, this study primarily investigated the influences of laser power and laser incident angle, two main factors, to understand the pattern of thermal stress and achieve precise control. When the laser beam was not perpendicular to the diamond coating surface, automatic focusing during the scanning process was achieved using a 3D scanning mirror.

A flywheel mechanical cleavage was employed to cleave the graphitized surface and achieve *in situ* transformation of graphite into graphene (figure 1(b)). To ensure uniform and effective cleavage force on the graphite, a flywheel made of steel was utilized, which underwent a mirror polishing treatment on its surface (diameter: 100 mm, thickness: 8 mm) [28]. Through preliminary experiments, the flywheel rotation speed was set at a higher value of 2000 rpm, and cleavage was

performed using the circumferential surface of the flywheel. The feed rate was set to $20 \text{ mm}\cdot\text{s}^{-1}$, and stable contact was ensured by applying appropriate small pressure. Moreover, a multidirectional cross-cleavage strategy was employed to ensure successful cleavage of graphite in multiple directions. Following the cleavage process, the samples were subjected to ultrasonic cleaning in anhydrous ethanol to remove impurities.

2.2. Numerical model

In order to effectively control the interfacial thermal stress during the graphitization process of diamond coatings and elucidate its influencing mechanisms, a two-dimensional finite element numerical model was established, and ANSYS was utilized to conduct finite element calculations. To improve computational efficiency while ensuring close agreement with experimental results, certain simplifications were made in the model construction: (i) the physical properties of the polycrystalline diamond coating and YG6 cemented carbide, such as thermal diffusion coefficient and specific heat capacity, were assumed to be isotropic. (ii) Due to the large size of the workpiece surface compared to the diameter of the laser beam waist and the variation in circular beam caused by laser source inclination, the Gaussian distribution of the laser heat source was approximated as a uniform surface heat flux density load, considering only the waist radius that contains 50% of the total laser power as the effective area of influence. (iii) The amplitude of the diamond surface contour was small, so it was assumed that the diamond surface was all located at the focal plane. The mesh of the diamond coating was refined ($0.2 \mu\text{m}$) to improve computational accuracy, while the mesh size of the carbide substrate was set to $1 \mu\text{m}$. Transient thermal analysis was performed using the two-dimensional plane element PLANE55, and transient thermal stress analysis was carried out using the PLANE42 element. In the atmospheric environment, the diamond surface undergoes graphitization at approximately $700 \text{ }^\circ\text{C}$ [29, 30]. Therefore, it was assumed that diamond elements exceeding $700 \text{ }^\circ\text{C}$ were 'killed' and considering that the fracture strength of YG6 cemented carbide was generally greater than 1450 MPa [31], the smaller value of 1450 MPa was set as the threshold for interfacial fracture. Additionally, the actual morphology of the diamond was considered in the model, rather than simplifying it to a smooth planar surface as commonly done in conventional operations. The material properties of the diamond coating and carbide substrate were allowed to vary in real-time with temperature to enhance the accuracy of the calculations.

2.3. Characterization

Field emission scanning electron microscope (SEM, ZEISS Gemini 300) was utilized to observe the surface morphology of the original diamond coating, graphitization, graphenization, and worn track. Raman microscopy (LabRam HR800, excitation wavelength 514 nm) was employed to detect and analyze the composition of the surface after graphitization and graphenization. Transmission electron microscopy (TEM,

FEI Talos-F200S) was used to observe and analyze the cross-sectional morphology and composition of the surface after graphenization. The graphitized diamond coating surface was annealed to remove the graphite phase change layer, and the surface roughness and graphitization depth were extracted using a 3D optical profiler (S Neox). The 3D optical profiler was also employed to extract the profile of the worn tracks and calculate the volume of wear. An optical video microscope was used to observe the wear morphology of the friction pins and evaluate the wear volume.

2.4. Friction tests and nanoindentation tests

High-speed reciprocating friction and wear tester (HSR-2M type, see table S1 for the technical parameters) was used to evaluate the lubrication and anti-wear properties of the precisely graphenized (PG) surface. Prior to the friction experiments, the samples and the SUS304 stainless steel friction pins with a diameter of 1.5 mm (figure S2) were ultrasonically cleaned in anhydrous ethanol to remove surface impurities. During the friction process, the frictional force generated between the friction pairs was continuously and automatically monitored, and converted into a COF for the entire testing cycle. The data acquisition rate was set at 1 Hz . The coated samples were fixed and reciprocated sliding against the friction pins in air ($22 \text{ }^\circ\text{C}$, $60\% \text{ RH}$). The sliding reciprocation length, number of sliding cycles, and reciprocation frequency were set at 2 mm , $24\,000$ cycles, and 6 Hz , respectively. In contrast to the conventional loads ($<10 \text{ N}$) used in existing literature for two-dimensional materials such as graphene as solid lubricants [22, 24, 25], larger loads ranging from 20 N to 150 N were applied to evaluate the friction characteristics of the PG surface, and compared with the original diamond coating surface. All the aforementioned experiments were repeated three times to ensure the repeatability of the experimental process.

Atomic force microscope (AFM, Nanonavill E-sweep) was employed to conduct nanoindentation tests on the PG surface in order to unveil its load-bearing characteristics. The probe material used was single-crystal silicon with a radius of 8 nm (PR-T300). The force constant of the probe's cantilever was $40 \text{ N}\cdot\text{m}^{-1}$, calibrated using the Sader method [32]. During the nanoindentation process, the probe displacement was sequentially set to 50 nm , 100 nm , and 200 nm . It is worth noting that the recorded indentation curves by the system represent the force-displacement relationship. Therefore, to obtain the force-indentation depth curve at the tip, it is necessary to take into account the flexural deformation of the probe's cantilever.

3. Results and discussion

3.1. Graphitization state of diamond coatings under different laser parameters

Conventional diamond coatings typically have a small thickness, usually not exceeding $10 \mu\text{m}$. Therefore, unlike diamond thick films and other diamond materials, achieving uniformly flat graphitization on the diamond coatings surface requires

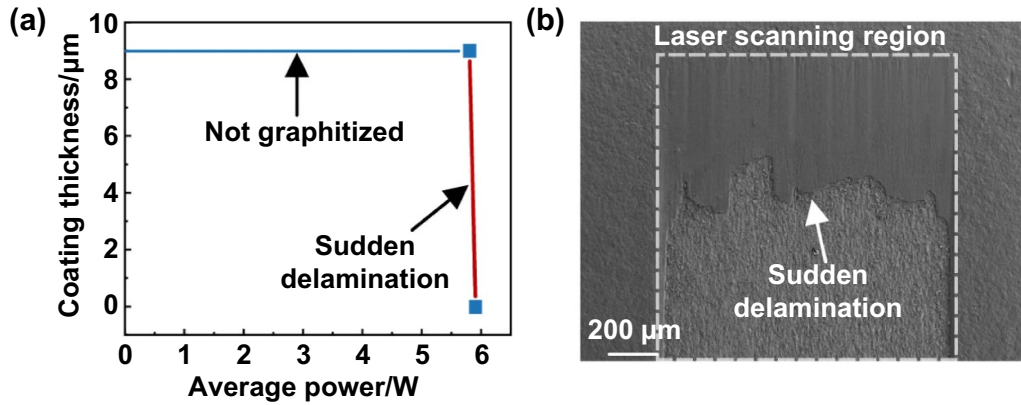


Figure 2. Sudden delamination of diamond coatings during the graphitization process. (a) Relationship between coating thickness and laser power at a 30° incident angle. (b) SEM image of the sudden delamination.

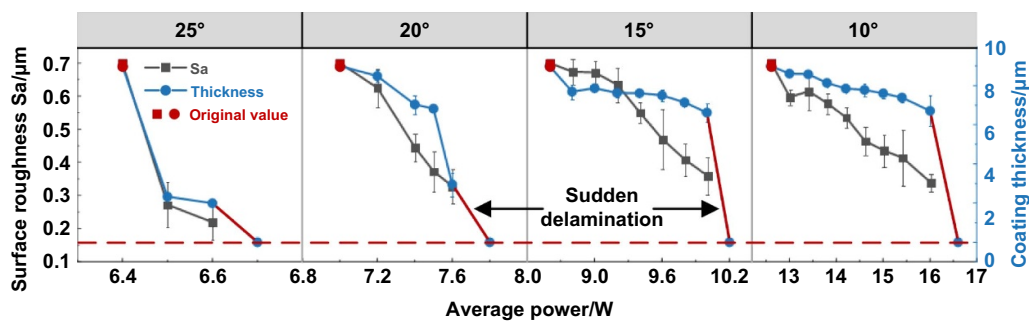


Figure 3. Influence of key laser parameters on the graphitization process of diamond coating surfaces at small incident angles.

considering the coating thickness and its impact on the substrate. When nanosecond laser irradiation is applied to diamond coatings, the coatings are prone to sudden delamination, especially at large laser incident angles θ_1 (90°–30°, the angle between the laser beam and the machining plane), making it challenging to achieve controlled graphitization of the diamond coatings. As shown in figure 2(a), at an incident angle θ_1 of 30°, no significant graphitization was observed within the laser power range of 0–5.8 W. When the laser power increased by 0.1 W, graphitization started on diamond coating surface. However, in the early stage of the graphitization process, the diamond coating experienced sudden delamination (figure 2(b)). As the incident angle θ_1 gradually decreased to 25°, controlled graphitization became evident on the diamond coating surface (figure 3). Furthermore, as the incident angle decreased, the range of controlled graphitization increased. For instance, at an incident angle of 25°, the average power range for controlled graphitization on the diamond coating surface was 0.3 W. However, when the incident angle θ_1 decreased to 10°, the range increased by an order of magnitude to 4 W. Correspondingly, the initial graphitization threshold power for the diamond coating also increased as the incident angle θ_1 decreased. For example, at an incident angle θ_1 of 25°, the initial graphitization threshold power was 6.4 W, whereas when the incident angle θ_1 decreased to 10°, the initial graphitization threshold power approximately doubled to

12.6 W. Additionally, from figure 3, it can be observed that at an incident angle θ_1 of 25°, the graphitization depth of the coating varied significantly with changes in laser power near the graphitization threshold. Specifically, with an increase of only 0.1 W in average power, the thickness of the graphitization coating decreased from 9 μm to 2.3 μm. This corresponds to the difficulties encountered in achieving controllable graphitization of diamond coatings using nanosecond laser in conventional vertical scanning mode and with larger incident angles. Conversely, at smaller incident angles θ_1 (15°, 10°), a different pattern emerged. The thickness of the non-graphitized coating showed a relatively gradual change with laser power initially, followed by a sudden delamination phenomenon. For example, at a small incident angle θ_1 of 15°, when the laser power increased from 8.6 W to 10 W, the diamond coating thickness only decreased by 2.37 μm. However, with a further increase of 0.2 W, the diamond coating was directly delaminated. As for surface roughness, it decreased with an increase in laser power within the range of controlled graphitization. Therefore, unlike diamond thick films, the graphitization process of diamond coatings under nanosecond laser irradiation exhibits complex laws. Ultimately, the selection of laser parameters should be based on the specific application scenarios, taking into account both the coating thickness and the surface roughness after flat graphitization.

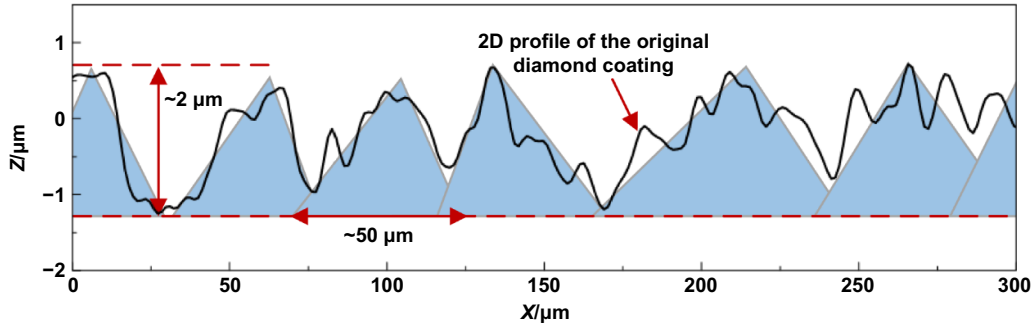


Figure 4. 2D profile of the original diamond coating surface. The black line is the extracted real profile line, and the blue triangles are the approximate fitted pyramid shape.

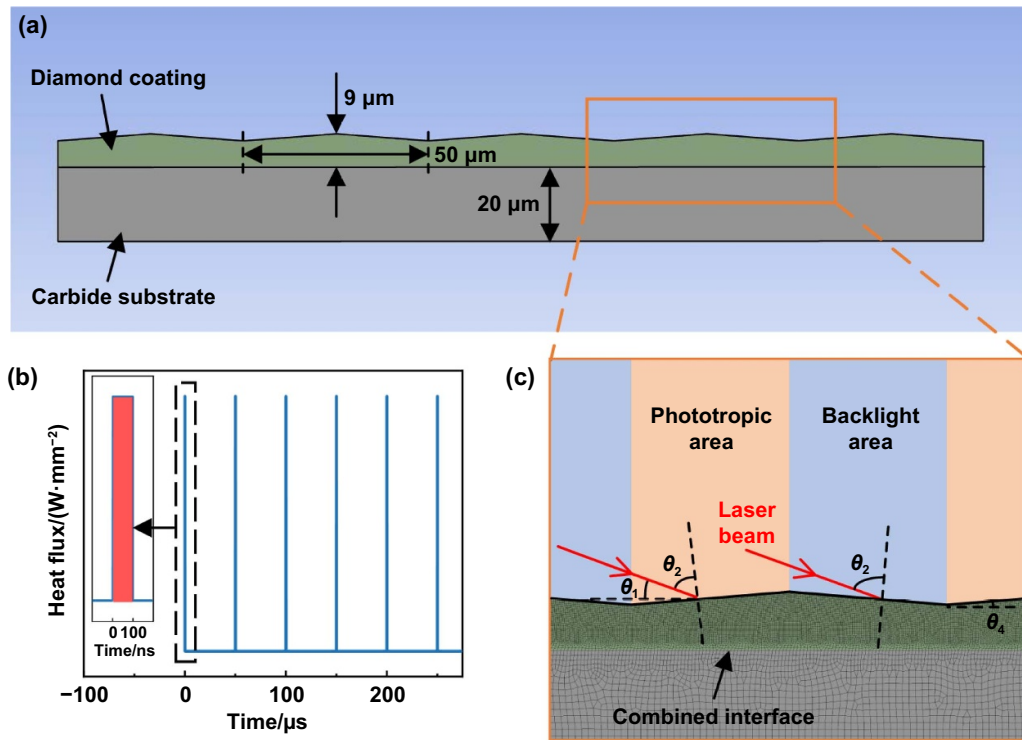


Figure 5. Rapid graphitization model of diamond coating under nanosecond laser irradiation. (a) Dimensions and structure of the model. (b) Loading pattern of surface heat flux density. (c) Angular relationship between different surfaces of the diamond coating and the laser beam.

3.2. Calculation of interfacial thermal stress during the graphitization process

According to section 3.1, unlike diamond thick films, the rapid graphitization of diamond coatings induced by nanosecond laser is accompanied by sudden delamination, exhibiting more complex behaviors and patterns. To elucidate the underlying mechanisms, it is necessary to clarify the temperature and thermal stress fields of the coating in the depth direction under nanosecond laser irradiation. Considering that the coating thickness is significantly smaller than its lateral dimension, this study established a corresponding two-dimensional finite element numerical model based on the extracted 2D profile of the original diamond coating surface (figure 4) through reasonable simplification (figure 5). The thickness of the diamond coating in the model was set to 9 μm, while the YG6 carbide

substrate had a thickness of 20 μm (figure 5(a)). Different from the vertical irradiation of laser, tilting the laser source would cause the circular beam spot on the coating surface to become elliptical. The major axis radius of the elliptical beam spot, corresponding to the waist radius $r_{50\%}$ that encompasses 50% of the total beam power, was denoted as r_{θ} (equation (1)):

$$r_{\theta} = r_{50\%} / \sin \theta_1 \quad (1)$$

where θ_1 is the angle between the laser beam and the horizontal plane of the workpiece, as mentioned previously. From the perspective of light propagation, the total laser energy $I_{T\theta}$ can be divided into two parts (equation (2)):

$$I_{T\theta} = I_{I\theta} + I_{R\theta} \quad (2)$$

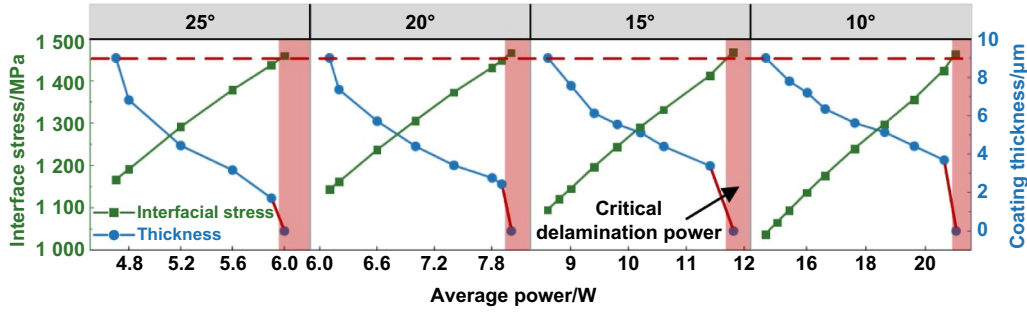


Figure 6. Theoretical calculation results of the influence of key laser parameters on the surface rapid graphitization process of diamond coating under the coupling effect of temperature and thermal stress field.

where $I_{I\theta}$ and $I_{R\theta}$ are the laser energy entering the diamond and the laser energy lost due to reflection, respectively, at the laser incident angle θ_1 . Since the pulse duration of the nanosecond laser is longer than the thermal diffusion time of the lattice, the action mode of nanosecond pulse laser ablation on diamond is dominated by heat [16, 33], that is, the laser energy is converted into heat, which is absorbed and diffused within the diamond coating. Therefore, the equivalent heat flux density q_θ absorbed on the diamond coating surface can be obtained from the following formula (equation (3)):

$$q_\theta = A * I_{I\theta} \quad (3)$$

where A is the ratio of absorbed thermal energy to the laser energy entering the diamond coating. When vertically irradiated with near-infrared laser at a wavelength of 1064 nm, the ratio of absorbed thermal energy to the total laser energy ranges from 0.15 to 0.16 [34]. Corresponding to the pulse mode of nanosecond laser, the loading form of the equivalent heat flux density on the diamond coating surface was depicted in figure 5(b). Under uniform beam irradiation, the rough surface morphology divided the surface into phototropic and backlight areas (figure 5(c)), resulting in different surface reflections and noticeable Fresnel phenomena [35]. Therefore, considering the coupling effect of inclined laser incident and surface roughness of the diamond coating, the energy loss due to reflection can be expressed as (equations (4)–(9)):

$$I_{R\theta} = R(\theta) * I_{T\theta} \quad (4)$$

$$I_{T\theta} = \frac{P}{\pi r_\theta * r_{50\%} * f * \tau} \quad (5)$$

$$R(\theta) = \frac{1}{2} [R_S(\theta) + R_P(\theta)] \quad (6)$$

$$R_S(\theta) = \left| \frac{n_1 \cos \theta_2 - (n_2 - ik_2) \cos \theta_3}{n_1 \cos \theta_2 + (n_2 - ik_2) \cos \theta_3} \right|^2 \quad (7)$$

$$R_P(\theta) = \left| \frac{n_1 \cos \theta_3 - (n_2 - ik_2) \cos \theta_2}{n_1 \cos \theta_3 + (n_2 - ik_2) \cos \theta_2} \right|^2 \quad (8)$$

$$n_1 * \sin \theta_2 = n_2 * \sin \theta_3 \quad (9)$$

where $R(\theta)$ is the proportion of reflected light energy to the total light energy, P is the laser average power, f is the laser pulse frequency, τ is the pulse width, $R_S(\theta)$ and $R_P(\theta)$ are

the components of the vertically and horizontally polarized light, respectively [35, 36]. n_1 is the refractive index of near-infrared light with a wavelength of 1064 nm in air, n_2 and k_2 are the refractive index and extinction coefficient of near-infrared light with a wavelength of 1064 nm in graphite, respectively. θ_2 is the angle between the incident light and the normal to the irradiated plane, and θ_3 is the angle between the refracted light and the normal to the irradiated plane. For the phototropic area, the following relation holds (equation (10)):

$$\theta_2 = 90^\circ - \theta_1 - \theta_4 \quad (10)$$

where θ_4 is the angle between the pyramid and its base. For the backlight area, the following relation holds (equation (11)):

$$\theta_2 = 90^\circ - \theta_1 + \theta_4. \quad (11)$$

In nanosecond pulse laser scanning, the overlap of pulse spots can result in repetitive ablation of the workpiece surface. Although the temperature of diamond reaches an equilibrium state within the first few pulses, at lower laser energy densities, the removal depth of the diamond surface exhibits a natural logarithmic relationship with the number of pulse spot overlaps [37]. Therefore, based on simulation calculated initial spot ablation depth $D_{1\theta}$, the increment in ablation depth $D_{N\theta}$ of subsequent overlapping spots can be expressed as a function of the number of spot overlaps N (equation (12)):

$$D_{N\theta} = D_{1\theta} * \left(\frac{\ln(N+1)}{\ln 2} - 1 \right) * \sin \theta_1. \quad (12)$$

The simulation results, as shown in figure 6, revealed that the non-graphitized thickness of diamond coatings during the controllable graphitization process was jointly determined by the depth of instantaneous high-temperature action and the thermal stress state at the interface. Therefore, the graphitization of diamond coatings should focus on two power limits: not only the graphitization threshold power but also the critical delamination power. Consistent with the experimental findings (figure 3), the controllable graphitization range significantly increased as the incident angle θ_1 of the laser decreased. At an incident angle of 25°, the theoretical calculation range for controllable graphitization power was 1.3 W, while it expanded to 6.9 W as the incident angle

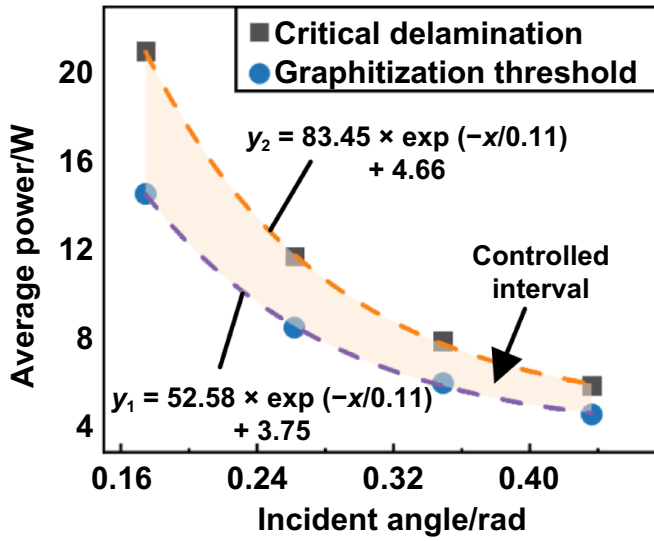


Figure 7. Statistical analysis and fitting of the graphitization threshold power and critical delamination power of diamond coatings at different laser incident angles. The determination coefficients (R^2) of the fitting curves were all 0.99.

decreased to 10° . To better understand the influence of the graphitization process on the diamond coating, statistical analysis and fitting of the graphitization threshold power and critical delamination power were conducted at different incident angles (figure 7). Consequently, the corresponding fitting functions were obtained, which can be expressed as (equations (13) and (14)):

$$y_1 = 52.58 * \exp\left(-\frac{x}{0.11}\right) + 3.75 \quad (13)$$

$$y_2 = 83.45 * \exp\left(-\frac{x}{0.11}\right) + 4.66 \quad (14)$$

where y_1 is the graphitization threshold power, y_2 is the critical delamination power, x is the radian values of the laser incident angles θ_1 . The results showed that the initial graphitization threshold power exponentially increased with decreasing incident angle θ_1 . For example, at an incident angle of 25° , the theoretical calculation threshold for initial graphitization power was 4.7 W, which approximately tripled to 14.6 W as the incident angle decreased to 10° . Similarly, the critical delamination power also exponentially increased with decreasing incident angle θ_1 , and the increase was more significant. For instance, at an incident angle of 25° , when the diamond coating started to graphitize, the interface thermal stress reached 1167.2 MPa, and with a mere increase of 1.3 W in laser power, the interface thermal stress surpassed the interface fracture threshold. However, when the incident angle decreased to 10° , the interface thermal stress at the onset of graphitization was 1037 MPa, which was 100 MPa lower than that at an incident angle of 25° , and the interface thermal stress exceeded the fracture threshold only when the laser power increases by 6.9 W (figure 6). Under the action of nanosecond pulse lasers, the instantaneous high temperature caused a rapid

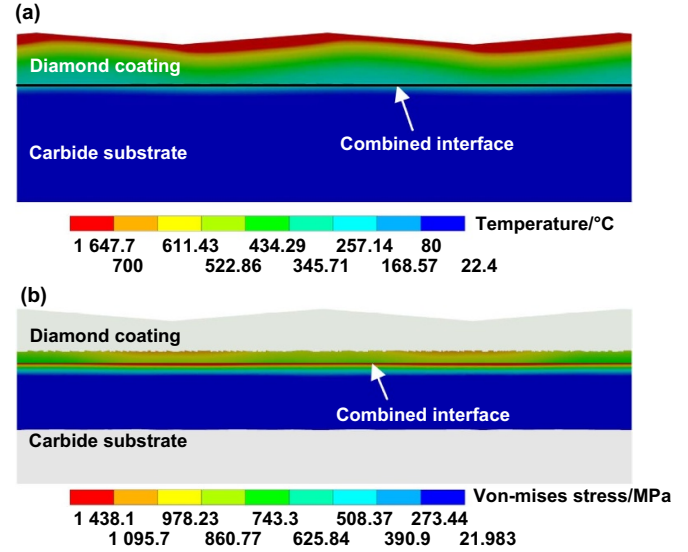


Figure 8. Cloud image during the rapid graphitization process of diamond coating. (a) Temperature distribution. (b) Thermal stress distribution at the interface between the coating and substrate.

rise in the surface temperature of the workpiece. When the temperature reached 700°C , the corresponding surface layer of diamond had undergone a transformation into graphite [29, 30]. Although the remaining diamond coating maintained its initial lattice structure, it experienced a relatively high temperature field due to its thinness. As a result, these high instantaneous temperature fields also caused a momentary increase in the temperature of the carbide near the interface (figure 8(a)). The transient temperature rises led to expansion of both diamond and carbide, and due to the significant difference in their coefficients of thermal expansion, a complex thermal stress field arose at the interface, potentially resulting in coating failure. The thermal stress field image at the interface shown in figure 8(b) demonstrated that the maximum thermal stress occurred in proximity to the interface, which explained the sudden failure of the diamond coating observed with an increase in laser power during the experiment. Therefore, during the rapid graphitization process, even though the diamond coating was not completely ablated, once the thermal stress at the interface exceeded the fracture threshold of the carbide, the entire coating would collapse directly.

Based on the results obtained from experiments and theoretical calculations, it can be observed that adjusting the laser incidence angle allows for effective control over the range between the graphitization threshold power and the critical delamination power, thereby achieving controllable graphitization of diamond coatings. The essence of this controllable graphitization lies in the regulation of absorbed energy within the diamond coating during the laser induction process. In the conventional nanosecond laser irradiation mode with vertical incidence, as the diamond coating surface gradually undergoes ablation, the laser energy propagates extensively downward along the beam direction. Due to the extremely low thickness of the coating, once the diamond surface reaches

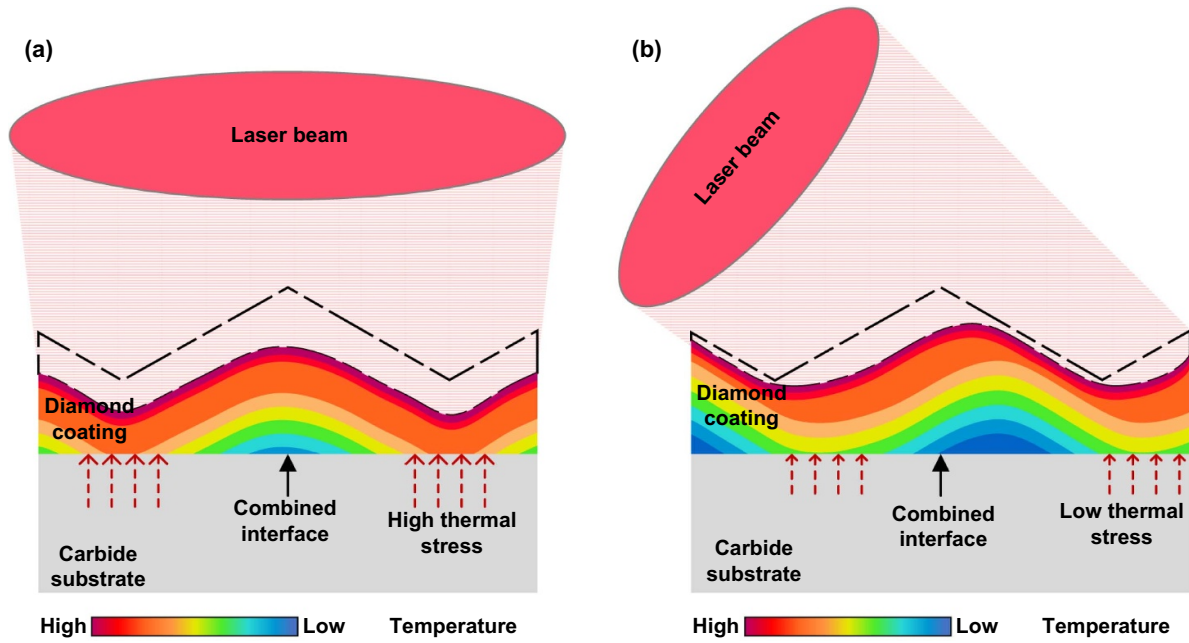


Figure 9. Schematic diagram of energy transfer control during the rapid graphitization process of diamond coatings induced by nanosecond laser. The diamond coatings are color-coded based on the temperature distribution. (a) Laser irradiation with vertical incidence. (b) Laser irradiation with a small incident angle.

the high temperature required for graphitization, the interface between diamond coating and carbide substrate also experiences a high-temperature field, resulting in significant interfacial thermal stress and ultimately leading to sudden delamination of the diamond coating (figure 9(a)). However, in the nanosecond laser irradiation mode with a small incident angle, the laser energy predominantly transfers laterally along the coating's depth direction due to the significant deviation between the beam propagation direction and the coating's depth direction. Additionally, the non-ideally smooth surface contour divides the diamond coating surface into phototropic and backlight areas. The backlight areas reflect a significant portion of the incident radiation, leading to uneven absorption of energy across the coating and intensifying the lateral transfer of absorbed energy (figure 9(b)). Consequently, this results in lower interfacial temperature and thermal stress, ultimately achieving stable graphitization of the diamond coating without causing damage to the metal substrate.

3.3. Precise graphenization under controlled interfacial thermal stress

Although the influence mechanism and control methods of surface graphitization and interfacial thermal stress have been obtained based on experiments and simulations, for achieving controlled graphitization of diamond coatings, further consideration is required to ensure the smoothness and uniformity of the graphenization for the good coverage of graphene. The surface morphology of the original diamond coating, as shown in figure 10(a), exhibited well-shaped diamond grains with an average size of approximately 500 nm. The corresponding Raman spectrum displayed a distinct diamond

peak (1330 cm^{-1}) and a weak G peak (1579 cm^{-1}), indicating the characteristic diamond structure (figure 10(b)). During the nanosecond laser irradiation process, when the graphitization depth of the diamond coating was less than $2\text{ }\mu\text{m}$, which was below the height of the 'pyramid' (figure 4), the base of the 'pyramid' could not be effectively machined, resulting in uneven localized graphitization. As shown in figure 10(c), after nanosecond laser treatment, certain regions of the surface exhibited distinct diamond grain contours, indicating minimal influence from the laser energy. This observation highlighted the significant reduction in the effective depth of laser-induced transient high temperatures brought about by the inclined nanosecond laser beam, which is crucial for controllable graphitization of thin diamond coatings. When the graphitization depth exceeded the height of the 'pyramid' ($2\text{ }\mu\text{m}$), the surface of the diamond coating could be uniformly graphitized, as shown in figure 10(d). After nanosecond laser treatment, the surface did not exhibit noticeable diamond grain contours but instead presented a consistent, loose powder-like structure, which was formed through laser-induced diamond graphitization followed by re-deposition. Further Raman spectrum analysis revealed four distinct characteristic peaks (figure 10(e)): the D peak (1360 cm^{-1}), the G peak (1577 cm^{-1}), the 2D peak (2712 cm^{-1}), and the D + D' peak (2936 cm^{-1}). The G peak is a typical feature of graphitization, while the D peak corresponds to the degree of disorder in the graphitized structure. The 2D peak is the second harmonic of the D peak [38, 39], with an I_D/I_G ratio of 0.79, indicating the presence of a loose powder structure on the surface composed of highly defective amorphous carbon. The low value of I_{2D}/I_G (0.12) suggested the presence of planar-oriented graphite components in the graphitized structure.

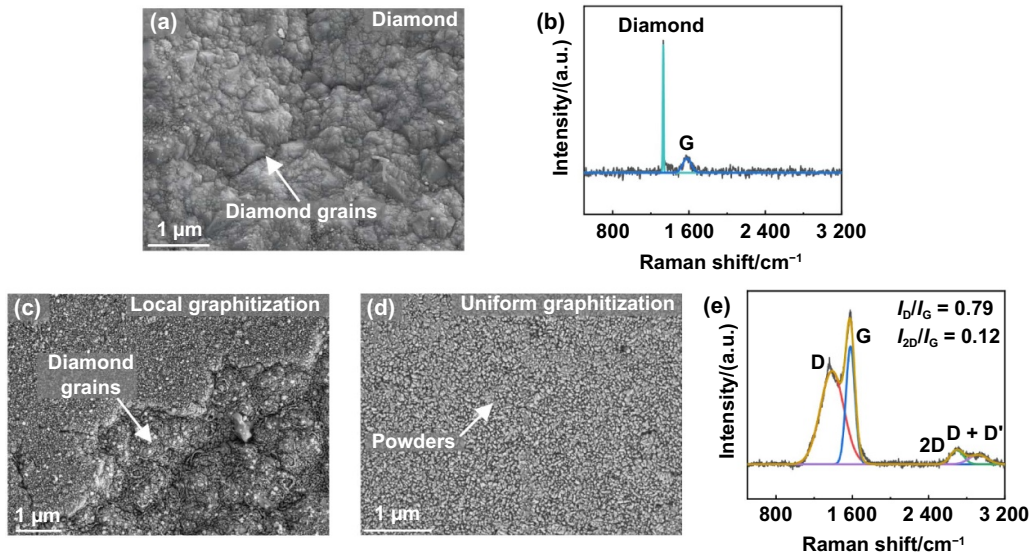


Figure 10. Surface morphology and composition of the diamond coatings during graphitization process. (a) and (b) SEM image and Raman spectrum of the original coating surface, respectively. (c) SEM image of the locally graphitized surface. (d) and (e) SEM image and Raman spectrum of the uniformly graphitized surface, respectively.

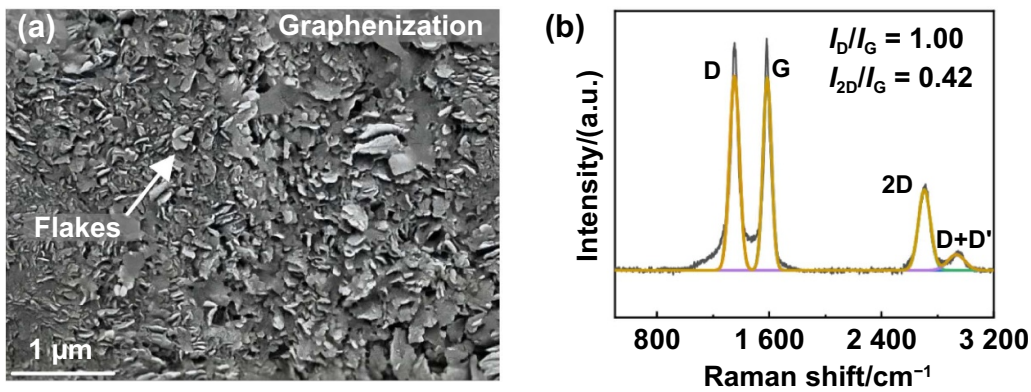


Figure 11. Surface morphology and composition after in situ graphenization. (a) SEM image and (b) Raman spectrum of the surface after in situ graphenization, respectively.

To demonstrate the broad applicability across different coating thicknesses, a uniformly graphitized surface with the extreme ablation thickness was selected for subsequent mechanical cleavage (processing methods can be found in the detailed Methods section). Specifically, a laser incident angle θ_1 of 10° and an average laser power of 16 W were selected, resulting in a thickness of $6.71 \mu\text{m}$ and a surface roughness S_a of $0.34 \mu\text{m}$ after uniform graphitization (figure 3). In contrast to the uniformly porous powder structure obtained after graphitization treatment, the final treatment resulted in densely packed flake structures on the PG surface (figure 11(a)). The lateral dimensions of the flakes were influenced by the size of the original diamond grains (figure 10(a)), and they were in the sub-micrometer range. Further Raman spectrum analysis revealed four prominent characteristic peaks: *D* peak (1352 cm^{-1}), *G* peak (1582 cm^{-1}), *2D* peak (2714 cm^{-1}), and *D + D'* peak (2945 cm^{-1}). Compared to the Raman spectrum of the graphitized surface (figure 10(e)), the I_{2D}/I_G ratio

significantly increased to 0.42 on the PG surface (figure 11(b)), indicating the densely packed flake structure as multilayer graphene. Simultaneously, the absence of prominent diamond characteristic peaks indicated good overall structure coverage. Additionally, a significant fraction of the *D* peak intensity can be attributed to the exposed edges of PG surface, resulting from the parallel alignment between the open edges of graphene sheets and the incident Raman laser beam.

To obtain a clearer understanding of the interface bonding state and structural components, cross-sectional TEM samples of the PG surface were prepared using focused ion beam technique. As shown in figure 12(a), the interface between the diamond coating and the carbide substrate exhibited excellent contact, indicating effective depth confinement of the instantaneous high temperature generated during nanosecond laser irradiation through parameter optimization. Additionally, the precise control over laser energy transfer, compared to the cracks generated on the diamond surface following laser

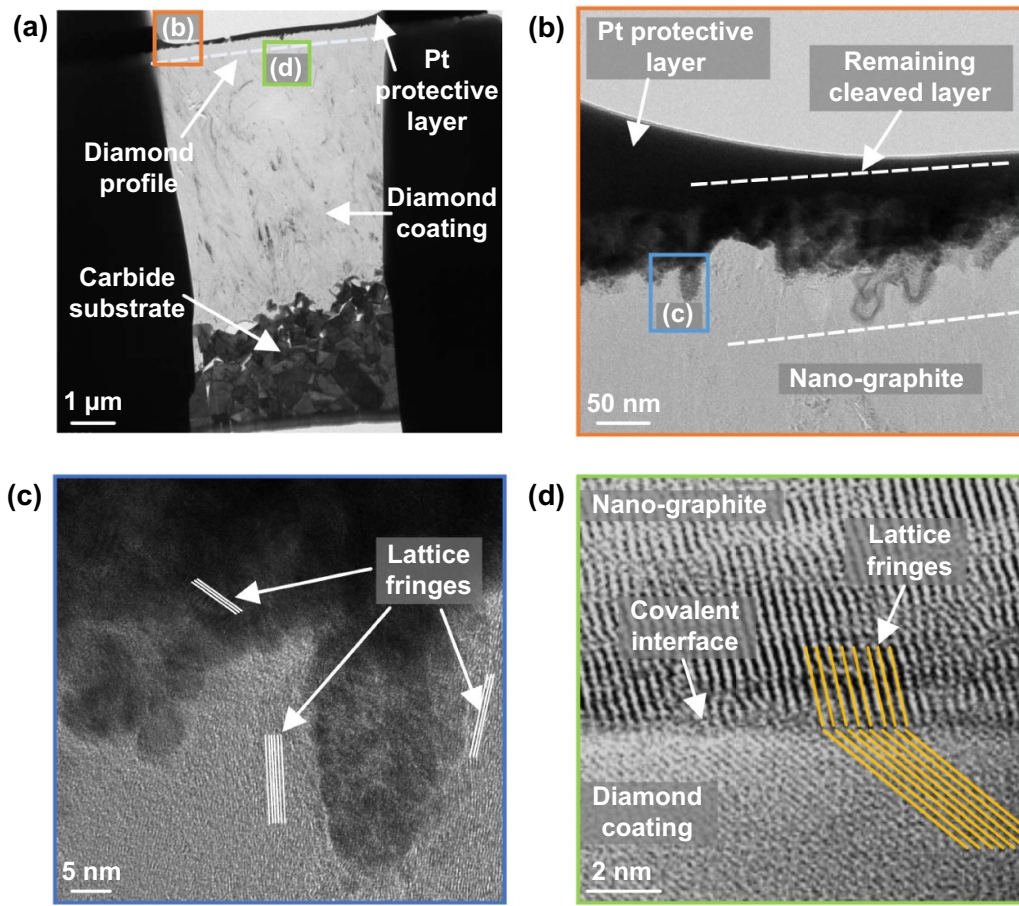


Figure 12. Cross-sectional morphology of PG surface. (a) Cross-sectional TEM sample of PG surface. (b) A magnified view of the upper surface in (a) to show more details. (c) HRTEM image of the remaining cleaved layer in (b). (d) HRTEM image of the interface junction in (a).

irradiation in the vertical direction (figure S3), maintained the integrity of the diamond coating's structure without significant surface or internal cracking (figures 10(d) and 12(a)). Due to the loose nature of the graphene structure on the upper surface and the significant hardness contrast with the underlying diamond, it was challenging to retain the graphene structure when thinning the sample to 50 nm using focused ion beam technique for TEM preparation. Nevertheless, residual cleaved layers can still be observed at higher magnifications in the TEM image of the upper surface. In figure 12(b), the upper portion of the residual cleaved layer exhibited a lighter color compared to the base, corresponding to the loose flake-like structure of graphene (figure 11(a)). Further investigation using HRTEM imaging (figure 12(c)) revealed well-defined lattice fringes in the cleaved layer, providing evidence of the typical layered structure of in situ graphene and induced graphitization. The root of the cleaved layer showed distinct cleavage traces and a vertically oriented orientation, which, being in close proximity to the diamond coating, served as transitional connections and consequently had a higher number of layers. Moreover, a dense nano-graphite layer existed

between the root of the cleaved layer and the diamond coating, with a height less than 200 nm (figure 12(a)). The vertically oriented nano-graphite layer exhibited regularly arranged on the crystal planes of the diamond coating with no apparent gaps at the interface (figure 12(d)), indicating the presence of covalent bonding between them. Further measurement of the interplanar spacing on this crystal plane revealed a value of 0.206 nm, corresponding to the (111) plane of diamond. Thus, precise graphenization of the diamond coating surface was achieved below the interfacial thermal stress threshold, enabling control over the thickness and roughness of the coating. Compared to the CVD method for the formation of high-bonding strength graphene on diamond surfaces, the proposed method in this study does not require high temperatures or special gas atmospheres, effectively suppresses the thermal stress between the coating and the carbide substrate, enabling the rapid preparation in ambient air. The low average power and shorter processing time required for the laser induction and mechanical cleavage involved in the method also contribute to reducing the carbon footprint during the preparation process.

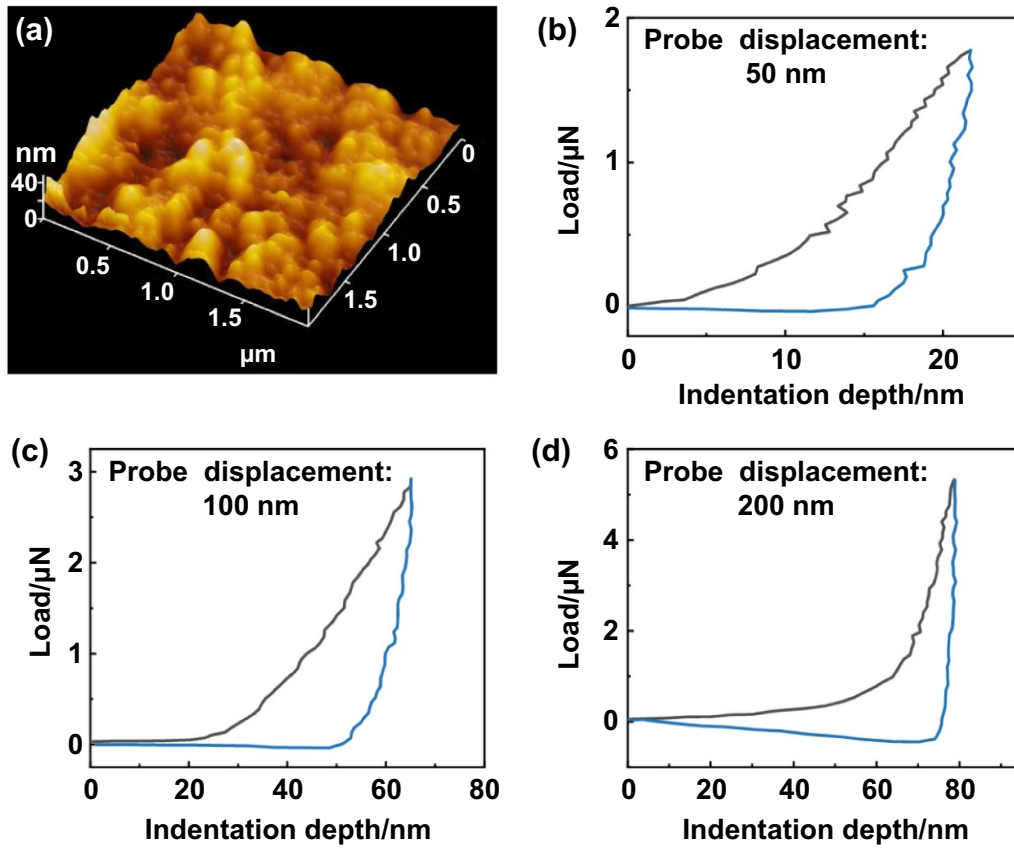


Figure 13. Load-bearing characteristics of PG surface. (a) AFM topography of PG surface. Force-depth curves obtained as the probe was lowered by (b) 50 nm, (c) 100 nm, and (d) 200 nm, respectively.

3.4. Mechanical properties

The aforementioned investigations indicated that PG surface consisted of loose graphene on top, followed by a vertically oriented nano-graphite layer, and the diamond coating at the base. These components exhibited vastly different mechanical properties but were integrated at the nanoscale. AFM possesses exceptional sensitivity to forces at the nanoscale and is commonly employed to measure the surface's micro-mechanical properties. Therefore, in this study, AFM was utilized to perform nanoindentation tests on the PG surface to characterize its load-bearing characteristics. The AFM topography of PG surface, as shown in figure 13(a), revealed a surface with a nanosheet structure corresponding to the loose graphene morphology. Figures 13(b)–(d) depicted the force-depth curves obtained as the probe was lowered by 50 nm, 100 nm and 200 nm, respectively. Due to the flexural deformation of the probe's cantilever, the actual indentation depth of the tip was smaller than the predetermined probe descent depth. At a small indentation depth of approximately 20 nm, the surface material exhibited evident viscoelastic behavior with a corresponding load of less than 2 μN (figure 13(b)). As the indentation depth increased by a factor of three to around 60 nm, the load only slightly increased to 3 μN (figure 13(c)), corresponding to the loose nature of the graphene sheets on the surface. However, when the indentation

depth further increased to 80 nm, the unloading curve became steep and nearly vertical (figure 13(d)), exhibiting characteristics of near-plastic deformation, corresponding to plastic deformation of the nano-graphite in the middle. Due to the nearly vertical arrangement of nano-graphite and the support provided by diamond, the corresponding load increased to approximately 6 μN , demonstrating a significant trend of high compressive resistance. Therefore, under compression at a scale of less than one hundred nanometers, the properties of the surface graphene and nano-graphite dominated, exhibiting distinct viscoelastic behavior. Under compression at greater depths, the properties of diamond became evident, showcasing exceptional compressive resistance.

Different from the conventional loads (<10 N) set in the existing literature using 2D materials as solid lubricants [22, 24, 25], this study evaluated the friction characteristics of the PG surface under heavy loads (50–150 N) and dry sliding conditions, comparing them with the original diamond coating. As shown in figure 14(a), during 24 000 reciprocating sliding cycles, the stable COFs of the original diamond coatings gradually decreased with increasing loads. This was attributed to the diamond's tendency to undergo graphitization/amorphization transition when subjected to ferrous metal friction and heavy load conditions, which provides effective self-lubrication but results in high surface wear [40]. In contrast, the stable COFs of the PG surfaces showed minimal

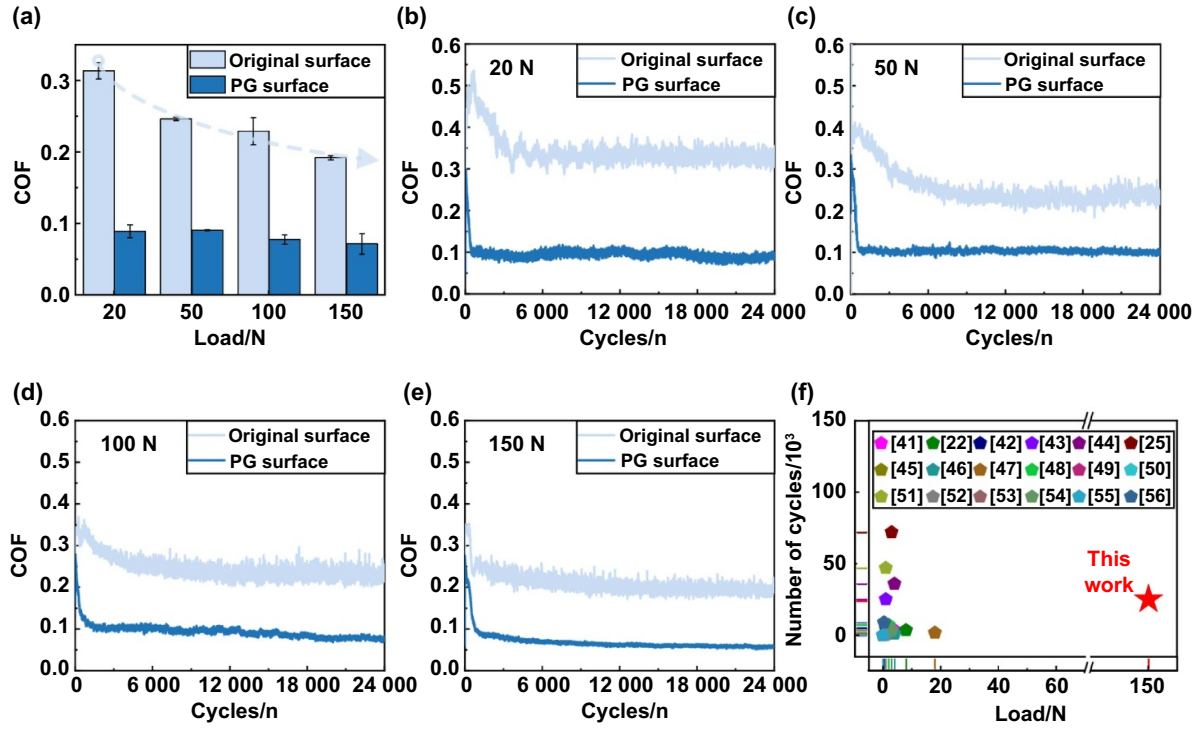


Figure 14. Lubrication characteristics of PG surfaces under different heavy loads (20 N–150 N), compared with the original diamond coating (dry friction, 24 000 reciprocating cycles). (a) Comparison of stable COFs. (b)–(e) Comparison of COF curves under loads of 20 N, 50 N, 100 N, and 150 N, respectively. (f) Comparison of this work with previous reports in terms of using graphene as a macro-scale solid lubricant on diamond surfaces under dry contact sliding [22, 25, 41–56].

Table 1. Comparison of this work with previous reports on the friction performance improvement of conventional diamond coatings under dry friction [17–20].

Surface roughness	Friction counterpart materials	Stable COF
164 nm	Steel/Tungsten carbide	0.38–0.42
120 nm	Steel/Titanium alloy	0.6
116 nm	Monocrystalline ruby	0.2
97 nm	Alumina	0.12
97 nm	Steel	0.25
5 nm	Steel/Titanium alloy	0.07
This work (340 nm)	Steel	0.06–0.09

variation with loads and remained below 0.1, exhibiting a significant reduction of 63%–72% compared to the original diamond coatings. Moreover, from the specific COF curves (figures 14(b)–(e)), the PG surfaces demonstrated less fluctuation compared to the original diamond coatings. Table 1 compared the improvement in friction performance of conventional diamond coatings under dry friction between this work and other studies [17–20]. Only when the surface roughness of the diamond coating decreased to a minimum of 5 nm, the stable COF was below 0.1 (0.07) in the case of dry friction against steel and titanium alloy. However, this cannot be widely applied due to the high cost and its inability to be used on practical engineering surfaces with various complex shapes. In contrast, in the precise graphenization strategy,

even with a higher surface roughness of 340 nm for the diamond coating, all stable COFs remained below 0.1, with the lowest reaching a remarkable 0.06. This collectively indicated that the strategy of precise graphenization effectively and cost-effectively improved the interfacial friction state and enhanced the lubrication performance of conventional diamond coatings. Particularly, previous studies have consistently shown a strong correlation between the durability of graphene solid lubricants on diamond surfaces and the applied load [22, 25, 41–56]. Most graphene solid lubricants tend to experience detachment failure after several hundred reciprocating cycles under high macroscopic loads, resulting in an increase in the COF curve. Figure 14(f) compared this work with previous reports using graphene as a macro-scale solid lubricant on

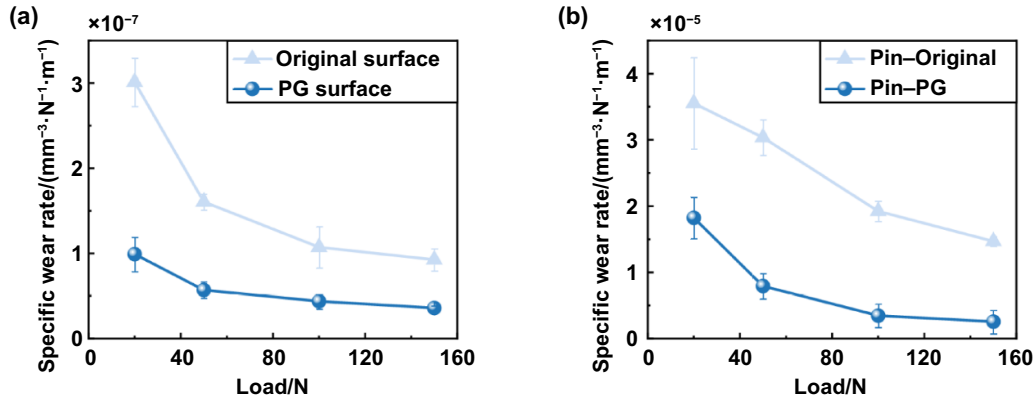


Figure 15. Wear characteristics of the friction pairs (20–150 N, dry friction, 24 000 reciprocating cycles). (a) Comparison of specific wear rates of the PG wear surfaces and original diamond coating wear surfaces. (b) Comparison of specific wear rates of the friction pins corresponding to the PG and original diamond coating.

diamond surfaces (the dimensions of the friction pin used in this study were similar to those of the friction ball/pin employed in the referenced literature), and the results demonstrated that the PG surface exhibited exceptional load-bearing capacity.

It is well known that diamond cannot machine ferrous metals, and when subjected to high friction with ferrous metals, it is prone to undergo graphitization/amorphization transition, leading to high wear [57–59]. This limitation severely restricts the application of diamond coatings on engineering surfaces. To verify whether the precise graphenization treatment in this study can suppress the mechanochemical wear of diamond coating surface, a typical ferrous metal, stainless steel (SUS304), was chosen as the friction counterpart. Under heavy loads (20–150 N) and dry sliding conditions, after 24 000 reciprocating sliding cycles, the worn volume of the coatings and the friction pins under different loads were measured. The specific wear rate w for each was calculated using the following formula (equation (15)) [60]:

$$w = \frac{V}{L * 2N * l} \quad (15)$$

where V is the wear volume of coating/friction pin, L is the applied load, N is the total cycles of sliding, l is the wear track length. According to figure 15(a), the specific wear rates of the PG surfaces were significantly reduced by 59%–67% compared to the original diamond coatings. The specific wear rates of the original diamond coatings showed a strong correlation with the applied loads, decreasing as the loads increased. In contrast, the specific wear rates of the PG surfaces were less affected by the loads. This indicated that the in situ graphenization treatment could effectively inhibit the mechanochemical wear of the diamond coating surface. Moreover, compared to the friction pins corresponding to the original diamond coatings, the specific wear rates of the friction pins corresponding to the PG surfaces were significantly reduced by 49%–83% (figure 15(b)). Furthermore, observations were made on the worn surfaces to understand the reasons behind the wear

differences. Under heavy load and dry sliding conditions, after 24 000 reciprocating sliding cycles, the diamond surface grains were ground and accompanied by a large amount of adhesions (figure 16(a)). In contrast, no significant adhesions were found on the PG surface, which still retained many flake structures on its surface (figure 16(b)). Additionally, under lower load conditions, the loose graphene on the PG surface appeared in a compacted state (figure S4), while still maintaining a denser fragmented structure compared to the state observed under higher load conditions. This indicated that an increase in load would accelerate the fracture of the flake structures. As for the friction counterparts, the worn surfaces of the friction pin corresponding to the original diamond coatings had many big pits, corresponding to the adhesions on the diamond coating surfaces (figure 16(c)), indicating significant adhesive wear on the friction pin surfaces. However, no significant big pits were found on the worn surfaces of the friction pin corresponding to the PG surfaces (figure 16(d)), indicating significant inhibition of adhesive wear on the surfaces, which was one of the main reasons for low friction and low wear performance. Additionally, the low wear of the friction counterparts corresponding to the PG surfaces could also be partially attributed to the smoother morphology of the diamond coating surface after precise graphenization [17–20]. Therefore, the strategy of PG not only effectively suppresses the mechanochemical wear of the diamond coating surfaces but also reduces the adhesive wear of the friction counterpart surfaces. This is of great significance for the widespread application of diamond coatings on sliding friction components such as mechanical seals and bearings.

4. Conclusions

In summary, derived from the idea of thermal stress control, this study overcomes the limitation of diamond coatings thickness and enables the in situ conversion of diamond coatings to graphene below the interfacial thermal stress threshold, while controlling the thickness and roughness of the coating.

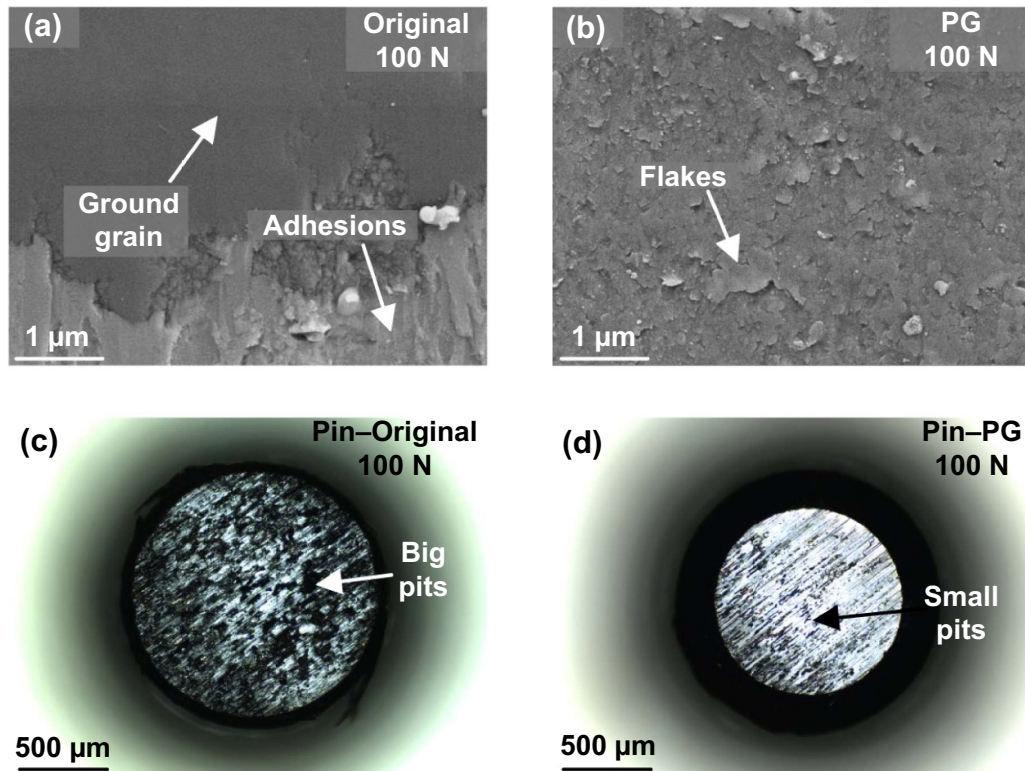


Figure 16. Topography of the worn surfaces (dry friction, 24 000 reciprocating cycles, 100 N load). (a) and (b) SEM images of the worn surfaces of original diamond coating and PG, respectively. (c) and (d) Optical topography images of the worn surfaces of the friction pin corresponding to the original diamond coating and PG, respectively.

The graphitization of diamond coatings induced by nano-second laser follows complex laws: within the controllable graphitization range, the surface roughness of the diamond coating decreases with increasing laser power; as the laser incident angle decreases, the range and initial power of controlled graphitization increase accordingly; at smaller incident angles, the graphitization depth of the diamond coating initially increases slowly with power, while at larger incident angles, the diamond coating is more prone to direct delaminate. Based on the original morphology of the diamond coating and considering the temperature and thermal stress field, a corresponding two-dimensional finite element numerical model is constructed. Two power limit formulas during the graphitization process are established by combining simulation calculations and experimental results. It is found that the graphitization threshold power and critical delamination power have an exponential relationship with the laser incident angle, elucidating the relationships and effects among laser parameters, coating thickness, surface morphology, and interfacial thermal stress. Ultimately, the influence of laser-induced transient high temperatures in the depth direction is effectively controlled, ensuring the integrity of the diamond coating, metal substrate, and bonding interface, and achieving precise graphenization of the diamond coating. Additionally, the friction properties of the resulting PG surfaces are evaluated under heavy loads (20–150 N) and dry friction. Compared to the original diamond coatings, the PG surfaces exhibits

a significant reduction in COFs by 63%–72%, all of which are below 0.1, with the lowest value reaching 0.06. The specific wear rates are also considerably reduced by 59%–67%, demonstrating superior lubrication and inhibition to mechanochemical wear. Moreover, the adhesive wear of the corresponding friction counterpart is significantly suppressed, with a substantial reduction in specific wear rates by 49%–83%. This work has the potential to enhance the performance of engineered surfaces with conventional diamond coatings, expanding their widespread use in sliding friction pairs requiring reduced friction and wear, such as cutting tools, bearings, and mechanical seals. Additionally, it holds promise for energy saving, emissions reduction, and achieving green manufacturing practices.

Acknowledgments

The authors gratefully acknowledge the support from the National Natural Science Foundation of China (NSFC) [No. 52475464, 52475463], National Natural Science Foundation of Jiangsu Province (No. BK20231442), the Fundamental Research Funds for the Central Universities (No. NS2024032), and the International Joint Laboratory of Sustainable Manufacturing, Ministry of Education and the Fundamental Research Funds for the Central Universities (No. NG2024007), China Scholarship Council (No. 202206830048), the Foundation of the Graduate Innovation

Center, Nanjing University of Aeronautics and Astronautics (No. kfjj20200510), and Funding for Outstanding Doctoral Dissertation in NUAU (No. BCXJ23-09).

ORCID iD

Ni Chen  <https://orcid.org/0000-0002-2036-0324>

References

- [1] Rouzbahani R, Pobedinskas P, Donatini F, Wong D, Pernot J and Haenen K 2024 Controlled boron content in lightly B-doped single crystal diamond films by variation of methane concentration *Carbon* **221** 118923
- [2] Yan B, Chen N, Xu C, Wu Y, Li L, Lee C and He N 2024 Covalently bonded heterostructures with mixed-dimensional carbons for suppressing mechanochemical wear of diamond under heavy loads *ACS Appl. Mater. Interfaces* **16** 19751–63
- [3] Chen N, Li H N, Wu J M, Li Z J, Li L, Liu G Y and He N 2021 Advances in micro milling: from tool fabrication to process outcomes *Int. J. Mach. Tools Manuf.* **160** 103670
- [4] Zhao G L, Zhao B, Ding W F, Xin L J, Nian Z W, Peng J H, He N and Xu J H 2024 Nontraditional energy-assisted mechanical machining of difficult-to-cut materials and components in aerospace community: a comparative analysis *Int. J. Extrem. Manuf.* **6** 022007
- [5] Fan S Y, Lin S S, Su Y F, Shi Q, Dai M J, Xiao S and Kuang T C 2023 Various HFCVD diamond coatings synergistically tuned using CH₄ gas flow and working pressure and key merit evaluation of their coated tools *Int. J. Refract. Met. Hard Mater.* **114** 106234
- [6] Sousa V F C and Silva F J G 2020 Recent advances on coated milling tool technology—a comprehensive review *Coatings* **10** 235
- [7] Yan B, He N, Chen N, Chen H, Sun S, Wu Y, Li L and Lee C 2024 Improving frictional state at fretting interfaces through the covalent structure of diamond–graphite–graphene *Tribol. Int.* **198** 109890
- [8] Handschuh-Wang S, Wang T and Tang Y B 2021 Ultrathin diamond nanofilms—development, challenges, and applications *Small* **17** 2007529
- [9] Peng J H, Zeng J W, Xiong C and Li L J 2020 The effect of interlayer reactivity on the quality of diamond coating by HFCVD deposition *J. Alloys Compd.* **835** 155035
- [10] Wang H, Song X, Wang X C and Sun F H 2021 Fabrication, tribological properties and cutting performances of high-quality multilayer graded MCD/NCD/UNCD coated PCB end mills *Diam. Relat. Mater.* **118** 108505
- [11] Li Z, Jiang F, Jiang Z Y, Tian Z G, Qiu T, Zhang T, Wen Q L, Lu X Z, Lu J and Huang H 2024 Energy beam-based direct and assisted polishing techniques for diamond: a review *Int. J. Extrem. Manuf.* **6** 012004
- [12] Luo H, Ajmal K M, Liu W, Yamamura K and Deng H 2021 Polishing and planarization of single crystal diamonds: state-of-the-art and perspectives *Int. J. Extrem. Manuf.* **3** 022003
- [13] Katamune Y, Murasawa K, Yoshitake T, Kikuchi T, Imokawa K and Ikenoue H 2023 Low-volume-loss surface polishing with a krypton fluoride excimer laser for polycrystalline diamond films *Appl. Phys. Lett.* **123** 031604
- [14] Prieske M and Vollertsen F 2021 Picosecond-laser polishing of CVD-diamond coatings without graphite formation *Mater. Today Proc.* **40** 1–4
- [15] Yan B, Chen N, He N, Wu Y, Zhang X L and Li L 2021 Surface modeling and component analysis of picosecond laser ablation of CVD diamond *Diam. Relat. Mater.* **111** 108191
- [16] Okamoto Y, Okubo T, Kajitani A and Okada A 2022 High-quality micro-shape fabrication of monocrystalline diamond by nanosecond pulsed laser and acid cleaning *Int. J. Extrem. Manuf.* **4** 025301
- [17] Pimenov S M et al 1996 Tribological properties of smooth diamond films *Appl. Surf. Sci.* **92** 106–14
- [18] Zhang D C, Shen B and Sun F H 2010 Study on tribological behavior and cutting performance of CVD diamond and DLC films on Co-cemented tungsten carbide substrates *Appl. Surf. Sci.* **256** 2479–89
- [19] Vandenbulcke L and De Barros M I 2001 Deposition, structure, mechanical properties and tribological behavior of polycrystalline to smooth fine-grained diamond coatings *Surf. Coat. Technol.* **146–147** 417–24
- [20] Bhushan B, Subramaniam V V, Malshe A, Gupta B K and Ruan J 1993 Tribological properties of polished diamond films *J. Appl. Phys.* **74** 4174–80
- [21] Chen S L, Lin Q, Ji Z, Sun Z Z and Shen B 2023 Ultrahigh mechanical robustness of vertical graphene sheets covalently bonded to diamond *Carbon* **201** 390–8
- [22] Chen S L, Shen B and Sun F H 2017 The influence of normal load on the tribological performance of electrophoretic deposition prepared graphene coating on micro-crystalline diamond surface *Diam. Relat. Mater.* **76** 50–57
- [23] Yuan Q L, Lin C T and Chee K W A 2019 All-carbon devices based on sp²-on-sp³ configuration *APL Mater.* **7** 030901
- [24] Won M S, Penkov O V and Kim D E 2013 Durability and degradation mechanism of graphene coatings deposited on Cu substrates under dry contact sliding *Carbon* **54** 472–81
- [25] Ji Z, Lin Q, Huang Z W, Chen S L, Gong P, Sun Z Z and Shen B 2021 Enhanced lubricity of CVD diamond films by in-situ synthesis of top-layered graphene sheets *Carbon* **184** 680–8
- [26] Smith P J, Chu B Y, Singh E, Chow P, Samuel J and Koratkar N 2015 Graphene oxide colloidal suspensions mitigate carbon diffusion during diamond turning of steel *J. Manuf. Process.* **17** 41–47
- [27] Chu B Y, Shi Y F and Samuel J 2016 Mitigation of chemical wear by graphene platelets during diamond cutting of steel *Carbon* **108** 61–71
- [28] Yan B et al 2023 Instantaneous formation of covalently bonded diamond–graphite–graphene with synergistic properties *Int. J. Mach. Tools Manuf.* **193** 104087
- [29] Komlenok M S, Kononenko V V, Ralchenko V G, Pimenov S M and Konov V I 2011 Laser induced nanoablation of diamond materials *Phys. Proc.* **12** 37–45
- [30] Kononenko V V, Konov V I, Pimenov S M, Prokhorov A M, Pavelyev V S, Soifer V A, Luedge B and Duparre M R 2002 Laser shaping of diamond for IR diffractive optical elements *Proc. SPIE* **4426** 128–34
- [31] Kang X Y, Lin N, He Y H, Zhang Q K, Zhang M M, Yan Y and Liu Y 2021 Improvement of microstructure, mechanical properties and cutting performance of Ti(C,N)-based cermets by ultrafine La₂O₃ additions *Ceram. Int.* **47** 19934–44
- [32] Sader J E, Chon J W M and Mulvaney P 1999 Calibration of rectangular atomic force microscope cantilevers *Rev. Sci. Instrum.* **70** 3967–9
- [33] Kononenko V V, Kononenko T V, Pimenov S M, Sinyavskii M N, Konov V I and Dausinger F 2005 Effect of the pulse duration on graphitisation of diamond during laser ablation *Quantum Electron.* **35** 252
- [34] Mei L F, Chen G Y, Zhang B, Chen G G and Huang K 2009 Measurement of YAG laser absorptance by artificial diamond and cubic boron nitride *Opt. Laser Technol.* **41** 770–7

- [35] Xie Y, Sengupta M, Habte A and Andreas A 2022 The “Fresnel equations” for diffuse radiation on inclined photovoltaic surfaces (FEDIS) *Renew. Sustain. Energy Rev.* **161** 112362
- [36] Rungasamy A E, Craig K J and Meyer J P 2021 A review of linear Fresnel primary optical design methodologies *Sol. Energy* **224** 833–54
- [37] Kononenko T V, Konov V I, Garnov S V, Klimentov S M and Dausinger F 2001 Dynamics of deep short pulse laser drilling: ablative stages and light propagation *Laser Phys.* **11** 343–51
- [38] Ferrari A C *et al* 2006 Raman spectrum of graphene and graphene layers *Phys. Rev. Lett.* **97** 187401
- [39] Chen N, Zhao J Y, Wang R K, Yan B, Wu Y, Li L, Yu N and He N 2024 Inhibition effect of covalent carbon nanosheets on mechanochemical wear of diamond *Mater. Des.* **237** 112573
- [40] Yuan S, Guo X G, Mao Q, Guo J, Van Duin A C T, Jin Z J, Kang R K and Guo D M 2021 Effects of pressure and velocity on the interface friction behavior of diamond utilizing ReaxFF simulations *Int. J. Mech. Sci.* **191** 106096
- [41] Chen S L, Shen B, Chen Y S and Sun F H 2017 Synergistic friction-reducing and anti-wear behaviors of graphene with micro- and nano-crystalline diamond films *Diam. Relat. Mater.* **73** 25–32
- [42] Chen S L, Shen B and Sun F H 2016 Enhanced tribological performance of CVD diamond films enabled by using graphene layers as solid lubricant *Adv. Mater. Res.* **1136** 573–8
- [43] Shen B, Hong H, Chen S L, Chen X and Zhang Z N 2019 Cathodic electrophoretic deposition of magnesium nitrate modified graphene coating as a macro-scale solid lubricant *Carbon* **145** 297–310
- [44] Shen B, Chen S L, Chen Y S and Sun F H 2017 Enhancement on the tribological performance of diamond films by utilizing graphene coating as a solid lubricant *Surf. Coat. Technol.* **311** 35–45
- [45] Bhowmick S, Banerji A and Alpas A T 2016 Friction reduction mechanisms in multilayer graphene sliding against hydrogenated diamond-like carbon *Carbon* **109** 795–804
- [46] Huang P, Qi W, Yin X, Choi J, Chen X C, Tian J S, Xu J X, Wu H C and Luo J B 2019 Ultra-low friction of a-C:H films enabled by lubrication of nanodiamond and graphene in ambient air *Carbon* **154** 203–10
- [47] Liu Y F, Li J J, Chen X C and Luo J B 2019 Fluorinated Graphene: a promising macroscale solid lubricant under various environments *ACS Appl. Mater. Interfaces* **11** 40470–80
- [48] Yin X, Wu F, Chen X C, Xu J X, Wu P, Li J J, Zhang C H and Luo J B 2020 Graphene-induced reconstruction of the sliding interface assisting the improved lubricity of various tribo-couples *Mater. Des.* **191** 108661
- [49] Kim K S, Lee H J, Lee C, Lee S K, Jang H, Ahn J H, Kim J H and Lee H J 2011 Chemical vapor deposition-grown graphene: the thinnest solid lubricant *ACS Nano* **5** 5107–14
- [50] Marchetto D, Held C, Hausen F, Wählich F, Dienwiebel M and Bennewitz R 2012 Friction and wear on single-layer epitaxial graphene in multi-asperity contacts *Tribol. Lett.* **48** 77–82
- [51] Berman D, Deshmukh S A, Sankaranarayanan S K R S, Erdemir A and Sumant A V 2014 Extraordinary macroscale wear resistance of one atom thick graphene layer *Adv. Funct. Mater.* **24** 6640–6
- [52] Matsumura K, Chiashi S, Maruyama S and Choi J 2018 Macroscale tribological properties of fluorinated graphene *Appl. Surf. Sci.* **432** 190–5
- [53] Huang Y H, Li Q Y, Zhang J, Qi Y Z, Wang H T, Zhao P and Meng Y G 2020 Effect of airborne contaminants on the macroscopic anti-wear performance of chemical vapor deposition graphene *Surf. Coat. Technol.* **383** 125276
- [54] Sun Y, Kandan K, Shivareddy S, Farukh F and Bailey R 2019 Effect of sliding conditions on the macroscale lubricity of multilayer graphene coatings grown on nickel by CVD *Surf. Coat. Technol.* **358** 247–55
- [55] Wu P, Li X M, Zhang C H, Chen X C, Lin S Y, Sun H Y, Lin C T, Zhu H W and Luo J B 2017 Self-assembled graphene film as low friction solid lubricant in macroscale contact *ACS Appl. Mater. Interfaces* **9** 21554–62
- [56] Liang H Y, Bu Y F, Zhang J Y, Cao Z Y and Liang A M 2013 Graphene oxide film as solid lubricant *ACS Appl. Mater. Interfaces* **5** 6369–75
- [57] Jiang G, Jianguo Z, Yanan P, Renke R K, Yoshiharu N, Paul S, Xiaobin Y, Baorui W and Dongming G 2020 A critical review on the chemical wear and wear suppression of diamond tools in diamond cutting of ferrous metals *Int. J. Extrem. Manuf.* **2** 012001
- [58] Wang J P, Zhang G Q, Chen N, Zhou M H and Chen Y B 2021 A review of tool wear mechanism and suppression method in diamond turning of ferrous materials *Int. J. Adv. Manuf. Technol.* **113** 3027–55
- [59] Komanduri R and Shaw M C 1975 Wear of synthetic diamond when grinding ferrous metals *Nature* **255** 211–3
- [60] Zeiler E, Klaffke D, Hiltner K, Grögler T, Rosiwal S M and Singer R F 1999 Tribological performance of mechanically lapped chemical vapor deposited diamond coatings *Surf. Coat. Technol.* **116–119** 599–608